



Microstructure and Tribological Properties of Plasma-Sprayed $\text{Al}_{0.2}\text{Co}_{1.5}\text{CrFeNi}_{1.5}\text{Ti}$ -Ag Composite Coating from 25 to 750 °C

Hang Li, Jianliang Li, Chengqi Yan, Xiafei Zhang, and Dangsheng Xiong

(Submitted April 28, 2019; in revised form February 16, 2020; published online March 4, 2020)

High-entropy alloys (HEAs) have been deliberated as potential matrix material for self-lubricating composites due to their excellent mechanical properties. In this study, the $\text{Al}_{0.2}\text{Co}_{1.5}\text{CrFeNi}_{1.5}\text{Ti}$ HEA powders with a face-centered cubic structure were prepared by mechanical alloying. Then, the alloyed HEA powders were sintered at 700 °C to achieve sprayed powder with suitable particle size. Next, the $\text{Al}_{0.2}\text{Co}_{1.5}\text{CrFeNi}_{1.5}\text{Ti}$ HEA-based composite coating was plasma sprayed on carbon steel by combining Ag. Dry friction experiment was applied in order to investigate the tribological properties of HEA – Ag composite coating at temperatures ranging from 25 to 750 °C. The composite coating that was sprayed with HEA – Ag exhibited a low friction coefficient (0.253) and a relatively low wear rate (8.9×10^{-6} mm³/Nm) at 750 °C. Furthermore, the HEA + Ag coating obtained an increased hardness and superior tribological properties after high temperature annealing. The dense, continuous oxide layer that was formed tightly covered the coating surface and combined with the lubrication of Ag clusters to protect the underlying materials from wear loss at high temperatures.

Keywords high-entropy alloy, lubricating composite coating, mechanical alloying, plasma spraying

1. Introduction

The exploration of self-lubricating materials over a wide temperature range has been an urgent task for decades that has not yet been completely accomplished (Ref 1-3). Until now, due to the good mechanical properties and thermal stability of metals or alloys, it has been an effective solution to achieve lubrication over a wide temperature range by taking them as matrix material in self-lubricating composite (Ref 4). Researchers have studied numerous metals or alloys at high temperatures, and they have obtained excellent tribological properties. This is especially true for the metal Ni (Ref 5-7) and its alloys (Ref 8-10). Additionally, metal-based materials play the role of load carrying and oxidation/wear resistance in composite materials, making the selection of matrix materials very important to improve the performance of self-lubricating composites.

Recently, a new alloy with multiple principal elements has led to the formation of “high-entropy alloys” (HEAs), which show many outstanding properties, such as high oxidation resistance (Ref 11, 12), high strength and hardness (Ref 11, 13), and excellent wear resistance (Ref 11, 14, 15). Furthermore, it is possible to take HEAs as matrix materials of self-lubricating composite. Previous researchers have reported that the HEAs

show various microstructures and mechanical properties, and as one of the simplest HEAs, the CoCrFeNi alloys with an FCC structure have been widely investigated (Ref 16, 17). On the basis of this information, researchers have also widely studied AlCoCrFeNiTi alloys (Ref 18-20) due to their enhanced mechanical properties. It has been reported FCC-based alloys show better higher workability but lower strength compared with BCC-based alloys (Ref 12). Additionally, by adding Ti atoms, the hard secondary phases that are formed can greatly increase in hardness and strength, like the Ni-Ti- and Ti-Co-rich phases. Also, the Al atom, which has a small atomic radius, can induce the formation of hard but brittle BCC phase and B2 compounds; the hardness can be reinforced due to the solution strengthening and hard phases. In addition, Al can easily generate a dense oxide film on alloy surfaces, and Ti has good corrosion resistance (Ref 20). Based on those facts, in this study, $\text{Al}_{0.2}\text{Co}_{1.5}\text{CrFeNi}_{1.5}\text{Ti}$ HEA was selected as the matrix material for designing self-lubricating composite coating, which has a high content Co and Ni to retain FCC structure and contains the addition of Al and Ti to improve the hardness of coatings.

It has been reported that thermal spraying is one of the effective methods to prepare high-entropy alloy coatings (Ref 21-23). Additionally, researchers have widely used the mechanical alloying process to synthesize HEA powders, from which the nano-crystalline can be easily obtained (Ref 24, 25). However, the powders obtained from the mechanical alloy have small particle sizes and poor flow abilities, making it difficult for them to be deposited during plasma spraying. Thus, the fine alloyed powders should be agglomerated to a larger particle to meet the requirement of spray powders. In this experiment, we used the sintering method as a common powder treatment to obtain suitable particle size for spraying (Ref 26-28). After sintered or thermal sprayed, whether or not the phase stability of sprayed Ag-HEA coating can be sustained is still ambiguous. The structure evolutions of alloyed powders and HEA coatings,

Hang Li, Jianliang Li, Chengqi Yan, Xiafei Zhang, and Dangsheng Xiong, School of Materials Science and Engineering, Nanjing University of Science and Technology, Nanjing 210094, China. Contact e-mail: jianliangli@163.com.

including phase transformation, grain size variation, and intermetallic phase segregation during plasma spraying and high temperature heating, both inevitably affected the tribological performance of composite coatings. It can be expected that the HEA powders and HEA coatings possess high structure stability during the preparation process and the tribology test, making the performance of HEA coating more reliable.

In this study, $\text{Al}_{0.2}\text{Co}_{1.5}\text{CrFeNi}_{1.5}\text{Ti}$ HEA was selected as matrix material for designing self-lubricating composite coating, and Ag was used as lubricant. The high-entropy alloy powders were prepared by mechanical alloying. The vacuum sintering process was adopted to obtain agglomerated powders with suitable particle size for spraying. Then, the composite coatings were prepared by plasma spraying technology. The tribological properties of HEA – Ag composite coating from 25 to 750 °C were investigated. And also their wear and lubrication behaviors were analyzed and discussed. For comparison, the tribological properties of $\text{Al}_{0.2}\text{Co}_{1.5}\text{CrFeNi}_{1.5}\text{Ti}$ coating, SUJ51, and Q125 steel were also tested at the same conditions.

2. Experiment Details

2.1 Materials and Methods

Al, Co, Cr, Fe, Ni, and Ti powders ($99.5\% \leq 45 \mu\text{m}$) with an atomic ratio of 0.2:1.5:1:1:1.5:1 were ball milled under argon atmosphere (purity 99.99%, pressure 0.5 MPa). The milling process was carried out in a high energy planetary ball miller with a 250 rpm rotating speed. The weight ratio of the ball to the powder was 10:1. The stainless steel balls with diameter of 5 mm and 10 mm as milling media were utilized. During ball milling, the powder samples at 0, 4, 8, 15, 30, 45, and 60 h were extracted for characterizing their structure by SEM. After milling for 60 h, the alloyed powders were sintered in a vacuum furnace ($5.5 \times 10^{-3} \text{ Pa}$) at 700 °C. Then, the powders were ground and sieved to obtain suitable particle size. The mass fraction of 95 wt.% $\text{Al}_{0.2}\text{Co}_{1.5}\text{CrFeNi}_{1.5}\text{Ti}$ and 5 wt.% Ag as-sprayed powders were mechanically blended, and then, subsequently the coatings on carbon steel were deposited by PS-1080 atmospheric plasma spray system. The spraying parameters are shown in Table 1. The $\text{Al}_{0.2}\text{Co}_{1.5}\text{CrFeNi}_{1.5}\text{Ti}$ coating was also prepared at the same conditions. The phase structures of powders and coatings were characterized by x-ray diffraction (XRD, D8 Bruker, Germany). The microstructure and chemical compositions of alloyed powders

Table 1 Plasma spraying parameters of the HEA and HEA – Ag composite coatings

Items	Value
Current	300 A
Voltage	28-32 V
Spray distance	100 mm
Argon flow rate	2600 L/h
Hydrogen flow rate	50 L/h
Powder feed rate	1 kg/h
Powder gas flow rate	0.4 m ³ /h
Spray gun walking speed	15 mm/s

and sprayed coatings were observed using scanning electron microscope (SEM, Quanta 250F, FEI, America) and the attached x-ray energy-dispersive spectrometer (EDS).

2.2 Hardness and Tribological Test

Before the wear test, the sprayed composite coatings were mechanically grounded with 600-grit emery paper and cleaned in acetone for 10 min. The tribological properties were investigated by a ball-on-disk high temperature tribometer with Si_3N_4 ball ($\phi = 6 \text{ mm}$) as upper specimen. The tests at a load of 5 N and a rotating radius of 5 mm were conducted, and the rotating speed was 300 r/min (around 0.157 m/s). Each friction test was sustained for 60 min (distance of 565.2 m), and the test temperatures were 25, 200, 400, 600, and 750 °C. Then, the morphologies of coatings' worn surface were observed by SEM, and a laser scanning confocal microscope (SM-1000) was used to calculate wear volume loss. The wear rates were calculated by $W = V/SF$, where V was the wear volume loss in mm³, S was the total sliding distance in m , and F was the applied load in N . Then, the chemical compositions and phases of worn surface were detected by EDS and Raman spectrum (HORIBA Scientific, Japan; laser wave number 532 nm). After the wear test at RT, 200, 400, 600, and 750 °C for 60 min in air atmosphere, the hardness of surface and unworn surface of the composite coatings was detected by a Vickers indentation test. The load was 2 N for 10 s, and at least 5 indents were conducted for each sample to obtain the average value.

3. Results

3.1 Characterization of Powders

Figure 1 shows the XRD patterns of $\text{Al}_{0.2}\text{Co}_{1.5}\text{CrFeNi}_{1.5}\text{Ti}$ powders at different milling times. The diffraction peaks of all constituent elements appear on the XRD of primitive mixed powders. Results show that the intensity decreased after milling for 2 h and then significantly decreased after milling for 8 h. Meanwhile, the diffraction peaks of Al disappeared after 8 h, which indicates the solid solution was formed. When the alloy powders were milled for 15 h, some weak peaks became

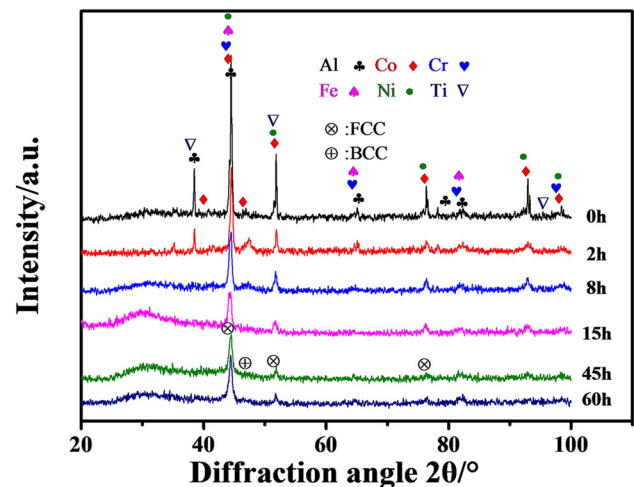


Fig. 1 XRD patterns of $\text{Al}_{0.2}\text{Co}_{1.5}\text{CrFeNi}_{1.5}\text{Ti}$ alloy powders at different milling times

invisible, and the preferred peak significantly broadened at about 45° . Additionally, the intensity decrement and broad of diffraction peaks resulted from the refined crystalline size, high lattice strain, and decreased crystallinity during mechanical alloying (Ref 29), while the disappearance of peaks was due to the formation of solid solutions. As the milling time increased to 45 and 60 h, only the most intense peaks can be observed, and a small amount of BCC phase existed in a measurable state, as shown in Fig. 1. This is because the mechanical alloying is a non-equilibrium process, which results in the formation of litter metastable BCC phase.

Figure 2 shows the morphologies of $\text{Al}_{0.2}\text{Co}_{1.5}\text{CrFeNi}_{1.5}\text{Ti}$ high-entropy alloy powders with different milling times. The primitive powders with particle sizes of less than $50\ \mu\text{m}$ were mechanically mixed. After milling for 8 h, larger particles were formed at the initial stage of mechanical alloying, and obvious cold welding and agglomeration between particles are observed in Fig. 2(b). The agglomeration was further intensified when the milling time extended to 15 h. The cold welded and agglomerated particles were crushed down and broken when mechanical alloying time increased to 30 h. The circulation of agglomeration and crushing refined the powders, which can facilitate the diffusion and alloying of different metallic elements. This equilibrium was achieved at a milling duration of 45 h. As shown in Fig. 2(e), the alloy powders reached an

average particle size of less than $5\ \mu\text{m}$ after grinding for 45 h. When milling time reached 60 h, the particle size had not significantly changed.

The EDS spectra are shown in Fig. 3, and the representative results are displayed in Table 2. The results show that the metal elements of alloyed powders particles had a uniform distribution and obtained similar atomic ratios with designed composition after ball milling for 60 h.

Table 3 shows the grain size and lattice strain of HEA powders with different milling times. Obviously, the grain size was refined with increasing milling time. Additionally, the average grain size of powders after mechanical alloying for 45 h was $19.8\ \text{nm}$, which was almost equal to that of powders after mechanical alloying for 60 h. This indicates that it becomes difficult to further refine the grain, and the equilibrium of grain refinement was achieved after 45 h. Meanwhile, there was a strong lattice strain in the powders during the mechanical alloying. This is due to the atoms' size mismatch of different alloy elements, the continuous increase in grain boundaries, and the serious mechanical deformation (Ref 30). The supersaturated solid solutions were formed in the powders after mechanical alloying for 45 h, and the enhancement of solid solubility was caused by the effect of high mixing entropy and the process of non-equilibrium of mechanical alloying (Ref 31, 32).

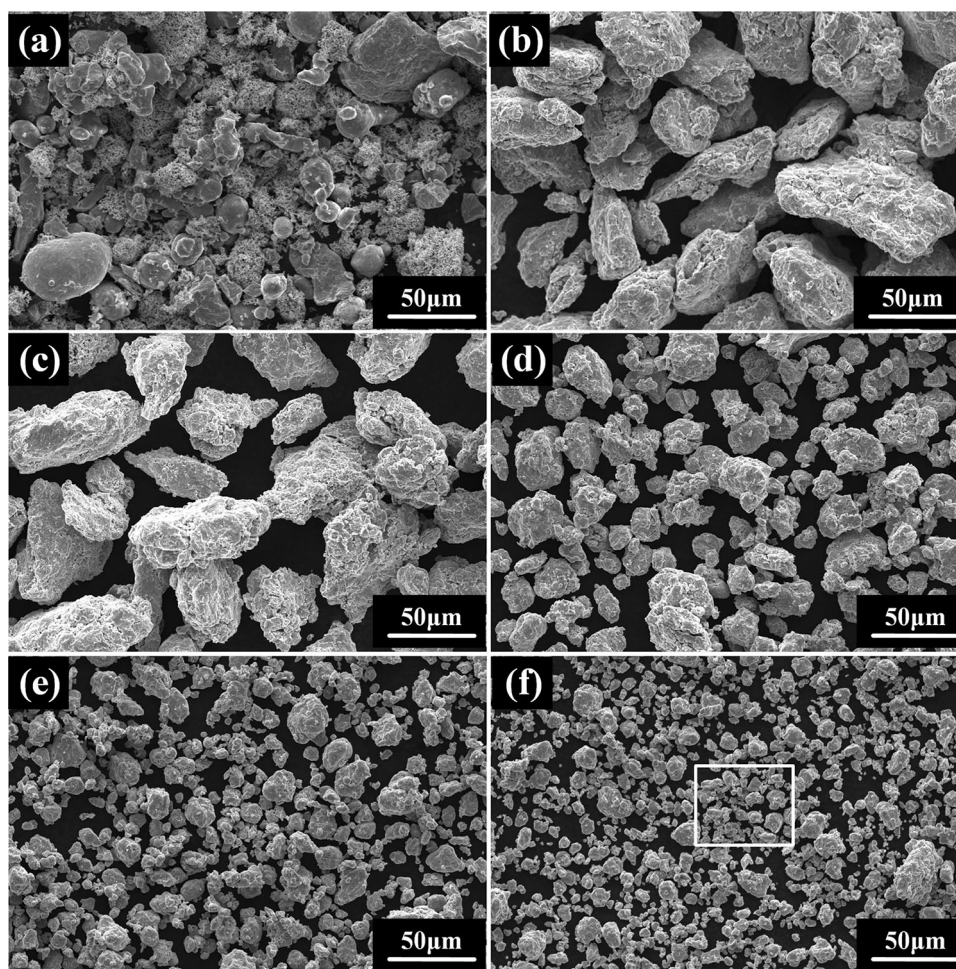


Fig. 2 SEM images of the mixed powders with different mechanical alloying times: (a), (b), (c), (d), (e), and (f), respectively, corresponding to 0, 8, 15, 30, 45, and 60 h

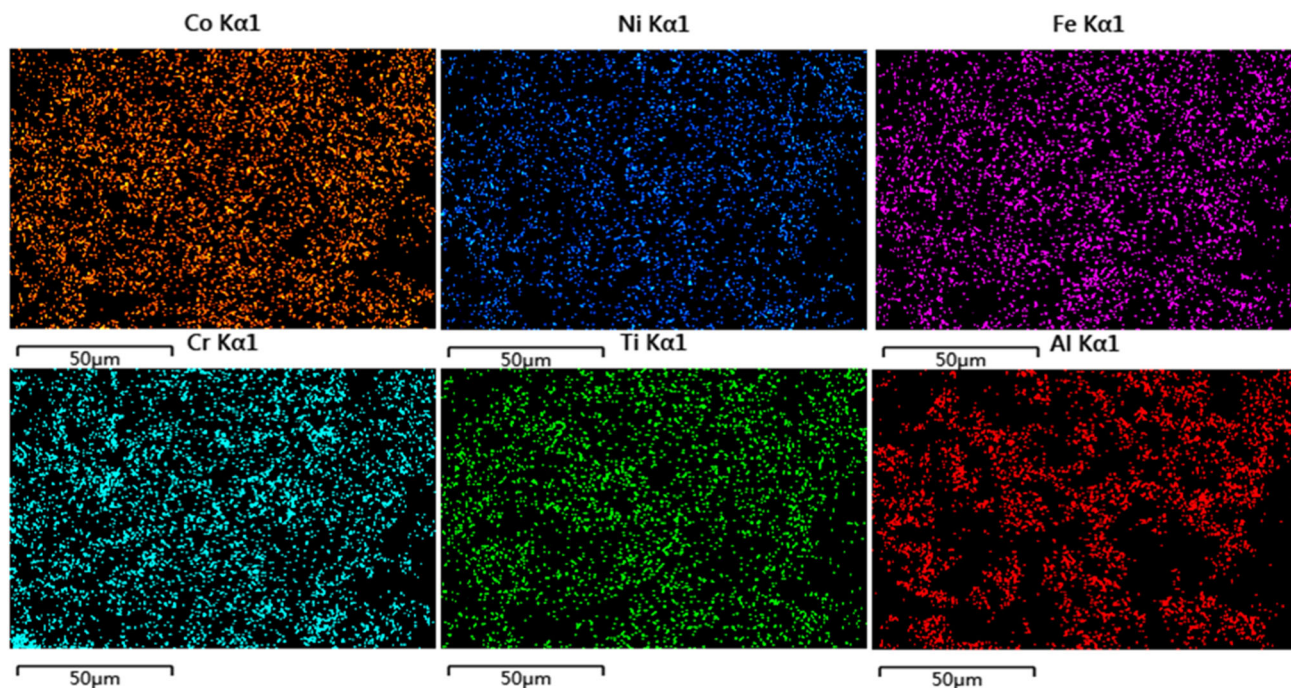


Fig. 3 Elements distribution images of Al, Co, Cr, Fe, Ni, and Ti of the mixed powders after mechanical alloying for 60 h

Table 2 Atomic percentage of the alloyed 60-h powder constituent elements

Element	Al	Co	Cr	Fe	Ni	Ti
Design, %	3.23	24.19	16.13	16.13	24.19	16.13
Actual, %	2.75	24.61	15.76	16.55	24.00	16.33

Table 3 Grain size and lattice strain of mixed powders under different mechanical alloying times

Sample	Mill time, h	Grain size, nm	Strain, %
1	15	29.6	0.2563
2	30	25.4	0.3011
3	45	19.8	0.4452
4	60	17.3	0.5329

Figure 4 presents the XRD patterns of powders and sprayed coating. From the XRD pattern of sintered powders, the tiny particles with high surface energy were agglomerated, and partial residual stress could be eliminated at the selected temperature of 700 °C. After sintering and grinding, the powders still maintained a stable FCC phase structure. The characteristic peaks of sprayed HEA – Ag composite coating mainly consist of Ag, a few oxides of Cr, and FCC phase of HEA, which indicates that Ag and alloyed HEA powders were successfully deposited, and the FCC phase and nano-crystalline structure of HEA powders was retained after spraying.

The cross-sectional morphologies of $Al_{0.2}Co_{1.5}CrFeNi_{1.5}Ti$ Ag composite coating are shown in Fig. 5. The deposited coating has a typical lamellar structure with a thickness of

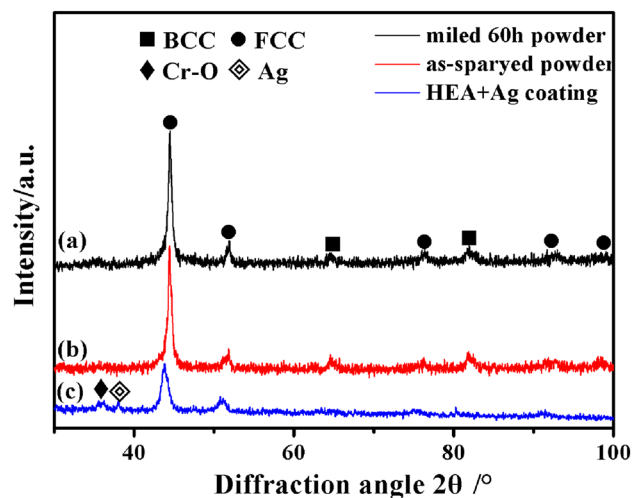


Fig. 4 XRD patterns of the mixed powders after mechanical alloying for 60 h (a), powders after sintering at 700 °C (b), and the sprayed HEA + Ag coating (c)

approximately 400 μm. Furthermore, the ribbon-like layers with little pores and cracks can be observed, and the particles presented good melting with a stripped distribution. In addition, Fig. 6 shows the element distribution of HEA – Ag composite coating; the enrichment of Cr and Ni elements can be observed. Few researchers have reported that the Cr-rich FCC phase existed in the CoCrFeNi HEA (Ref 16, 33). Due to the fact that the mechanical alloying process is non-equilibrium, some constituents could not be alloyed completely, and Ni-enriched area was formed.

Table 4 shows the micro-hardness of unworn and worn surface of HEA – Ag composite coating after wear testing at different temperatures. The hardness of cross section of sprayed coating was 620.06 HV, and for the same sample, the surface

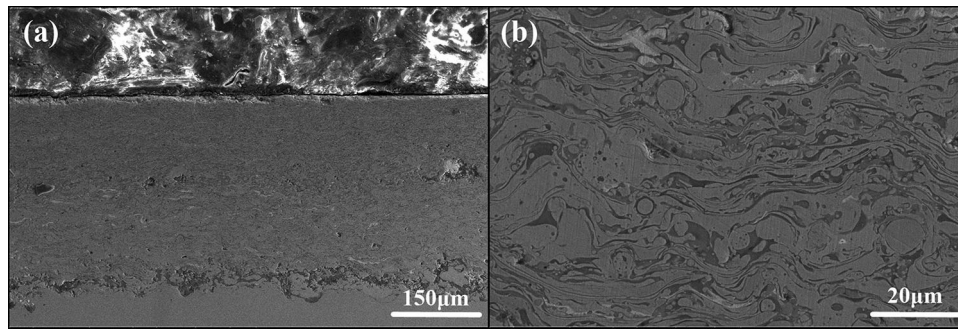


Fig. 5 SEM images of cross section of the deposited HEA + Ag composite coating

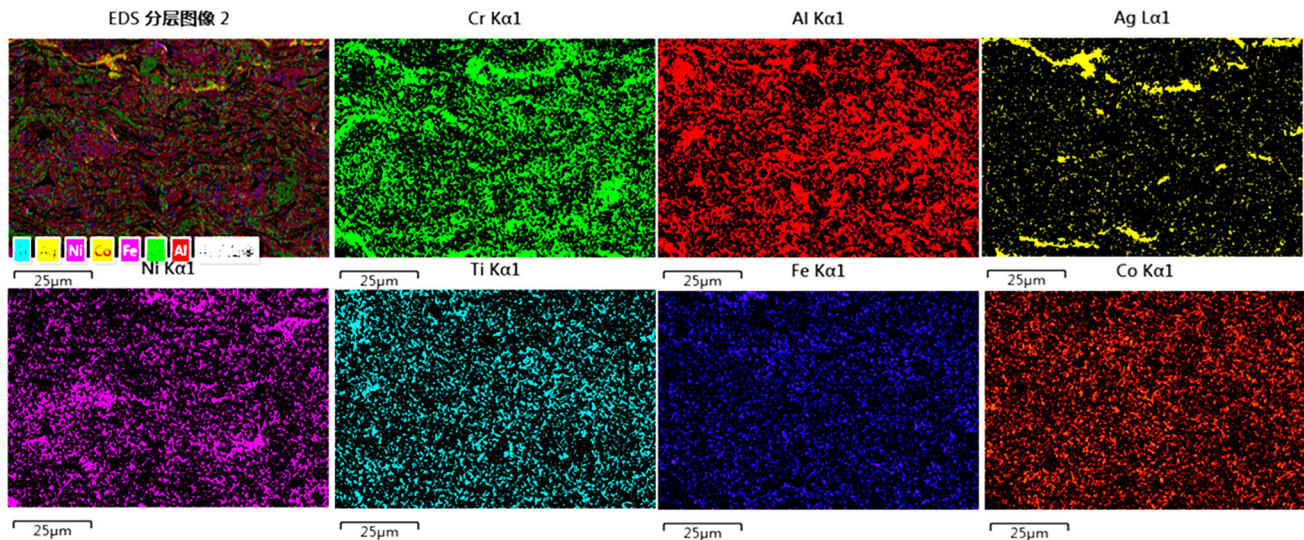


Fig. 6 Elements distribution images of Al, Co, Cr, Fe, Ni, Ti, and Ag of the deposited HEA + Ag composite coating

Table 4 Hardness of HEA – Ag composite coating (unit HV)

	Unworn surface	Worn surface
25 °C	392.56	420.05
200 °C	444.58	461.21
400 °C	538.20	574.71
600 °C	739.82	760.23
750 °C	756.28	786.62

hardness was much lower (390.6 HV). This significant difference is due to micropores on the surface of the deposited coatings, and the micro-pores structure is a common feature of the thermal spraying coatings. After the wear test at room temperature, the micro-hardness increased to 420.05 HV, which can be attributed to the compact structure and the formation of hard oxides. The surface hardness changed a little at 200 °C, and it linearly increased with increasing test temperature. Additionally, when the temperature rose to 750 °C, it sequentially increased to 739.8 HV. Meanwhile, the hardness of worn surface also increased, especially at high temperatures. The increased hardness of worn and unworn surface was mainly caused by oxidation. At first, the ultrafine grain structure of mechanical alloyed powders could be preserved on the

composite coating due to rapid cooling during plasma spraying. After the deposited coating annealed at high temperatures in air (Fig. 11), the number of annealed precipitation particles with nano-scales appeared. These particles were mainly composed of oxides, and the precipitation oxide particles that were formed can be attributed to grain growth and oxidation. In addition, from the XRD of unworn surface after annealing at different temperatures, it is obvious that oxide was formed on the surface and that the FCC structure was unchanged. The increased hardness was mainly caused by oxidation. In addition, the hardness could be enhanced by precipitation hardening, as in the Ni-Ti- and Co-Ti-rich phase. However, in contrast to the bulk HEA material, for the coatings with powder metallurgic method, the precipitation, phase boundary, and character of phase structure hardly can be observed in the SEM, and it is hard to see the precipitation phase in the XRD of Fig. 12. Compared with unworn surface, the higher hardness of worn surface can be attributed to high cyclic pressure and friction induced by oxidation, in which compact structures and hard oxides were formed.

3.2 Tribological Properties

The tribological properties of HEA and HEA – Ag composite coatings were investigated from room temperature to 750 °C. Figure 7(a) shows the friction coefficient curves of HEA and HEA – Ag composite coatings. After 10 min

running, the friction coefficient curves were relatively stable. At room temperature, the curve of HEA + Ag coating was rough and uneven (avg 0.43), which was caused by the abrasive wear of hard particles, as displayed in Fig. 9(a). Additionally, the curve of HEA coating was more stable, but the average coefficient was higher (avg 0.49) compared with HEA + Ag coating. In addition, the friction coefficient attained its highest value at 200 °C (avg 0.54 and 0.64). At this temperature, oxidation resistance plays a critical role in the mild oxidation wear mechanism. As shown in Fig. 9(c) and (d), the worn surface shows delamination of the oxide layer because the internal stress reached a critical thickness, the crushed oxide particles were distributed in the worn surface, and the continuous oxide film can't be formed. The coarse surface increased friction resistance, and a similar phenomenon appeared at 400 °C. The average friction coefficients were 0.457 and 0.616, respectively.

It is obvious that the friction coefficients of HEA – Ag composite coating were lower than HEA coating at 25–400 °C. This may be because the lubrication of Ag can effectively reduce friction resistance at this temperature range. As the test temperature increased to 600 and 750 °C, the friction coefficient of HEA – Ag composite coatings significantly decreased to 0.253 and 0.249, respectively. For both HEA and HEA – Ag composite coating, a relatively low friction coefficient value was obtained at high temperatures compared with PS400 coating (Ref 34, 35). Additionally, the addition of Ag had little effect on the friction coefficient of coating at high temperature. The main reason for the decreased in friction coefficients is that the wear form was changed, whereas adhesion and oxidative wear were the main mechanisms at high temperature. From Fig. 10, a denser, continuous oxide layer that formed and tightly covered on the coating surface for HEA and HEA + Ag coatings prevented the direct metal–metal contact and adhesive wear, reducing the friction force. The formed oxide layer can be observed from the SEM images, XRD, and Raman patterns.

Figure 8 shows the wear rate of HEA and HEA – Ag composite coatings at different temperatures. The wear rate of HEA coating was lower than $4 \times 10^{-5} \text{ mm}^3/\text{Nm}$ at RT and 200 °C, and it increased to its highest value ($12 \times 10^{-5} \text{ mm}^3/\text{Nm}$) at 600 °C before significantly decreased to $3.3 \times 10^{-5} \text{ mm}^3/\text{Nm}$ at 750 °C. The variation tendency of wear rate of HEA – Ag coating with increasing temperature was similar to that of HEA coating. At room temperature, the wear rate of HEA – Ag composite coating was about

$0.8 \times 10^{-5} \text{ mm}^3/\text{Nm}$, which was four times lower than that of the HEA coating. With increasing test temperature, the wear rate of HEA – Ag coating linearly increased ($5.89 \times 10^{-5} \text{ mm}^3/\text{Nm}$) at 600 °C and then significantly decreased to $8.9 \times 10^{-6} \text{ mm}^3/\text{Nm}$ at 750 °C. It is obvious that the wear rates of HEA – Ag composite coating were lower than of HEA coating at all temperatures. Meanwhile, the wear rates of HEA – Ag and HEA composite coating were much lower than those of SKH51 and Q125 steel, especially at high temperatures.

Figure 9 shows the SEM images of HEA and HEA – Ag coatings of worn surfaces from RT to 400 °C. As the test temperature increased, more and more flake wear debris particles with significant oxidation worn off. It was difficult to form a continuous oxide layer to resist wear, and the wear loss mainly came from the formed oxide debris. This corresponded with the increased wear rate with increasing temperature from 25 to 400 °C. Additionally, broken oxide debris was effectively relieved by the addition of silver. Figure 10 shows the SEM image of the worn surface of HEA and HEA – Ag at 600 and 750 °C. At both temperatures, they had a smooth surface. The surface was much smoother for the HEA – Ag coating at 600 and 750 °C, and the width of worn surface was significantly reduced at 750 °C. At high temperatures, the

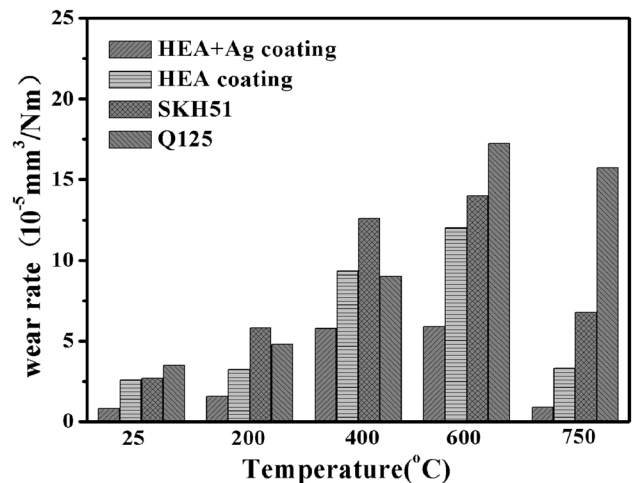


Fig. 8 Wear rate of composite coatings and SKH51, Q125 at different temperatures

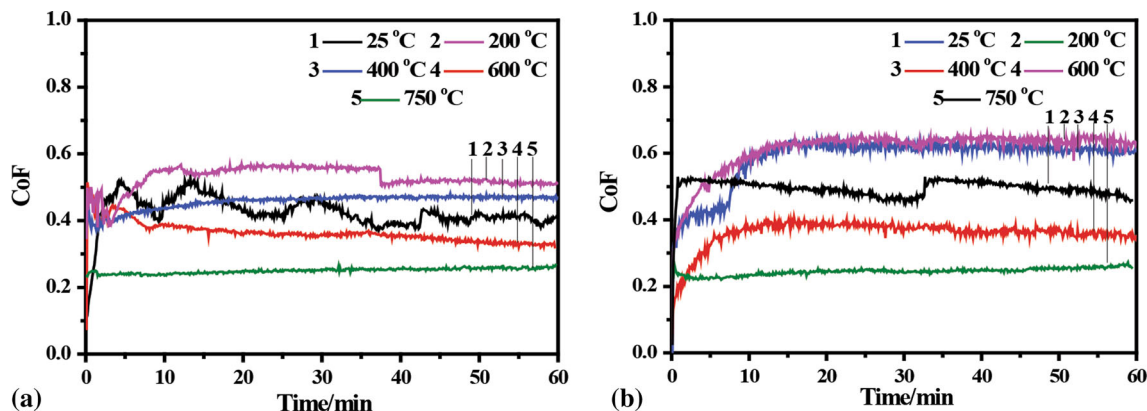


Fig. 7 Friction coefficient curves of $\text{Al}_{0.2}\text{Co}_{1.5}\text{CrFeNi}_{1.5}\text{Ti} + \text{Ag}$ coating (a) and $\text{Al}_{0.2}\text{Co}_{1.5}\text{CrFeNi}_{1.5}\text{Ti}$ coating (b) at different temperatures

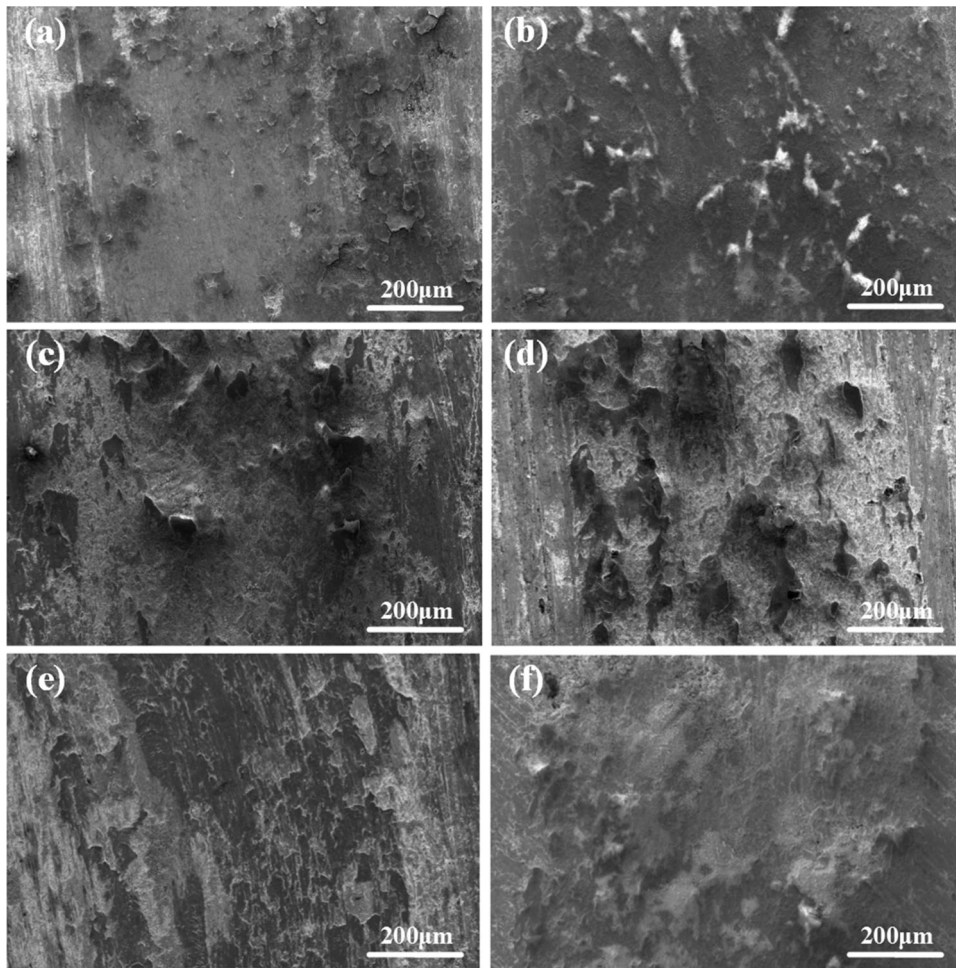


Fig. 9 Worn surface morphologies of the composite coatings: (a), (c), and (e) are the images of the $\text{Al}_{0.2}\text{Co}_{1.5}\text{CrFeNi}_{1.5}\text{Ti} + \text{Ag}$ coating at RT, 200, and 400 °C, and the (b), (d), (f) corresponding to $\text{Al}_{0.2}\text{Co}_{1.5}\text{CrFeNi}_{1.5}\text{Ti}$ coating at RT, 200, and 400 °C

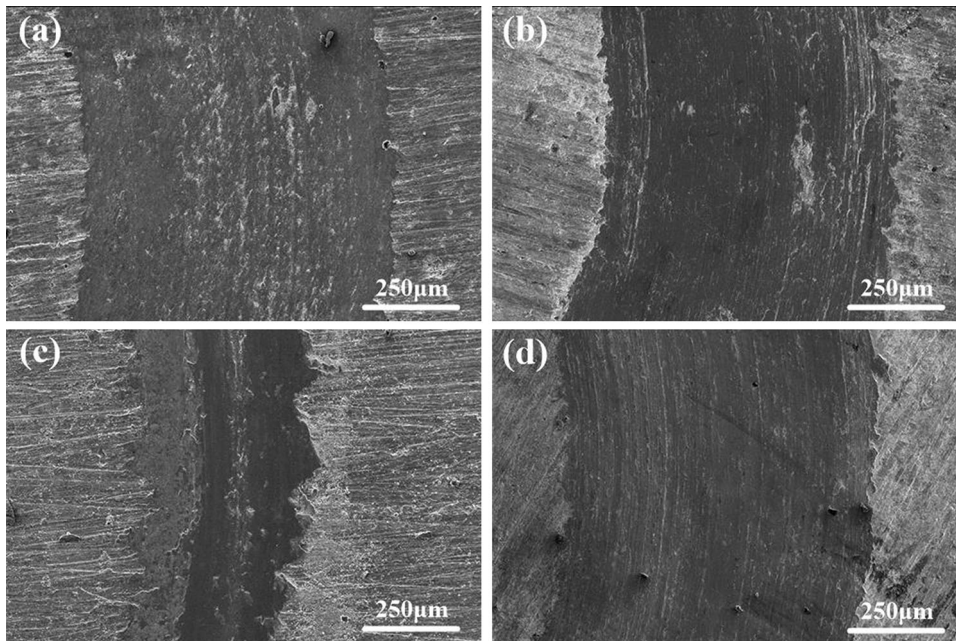


Fig. 10 Worn surface morphologies of composite coatings: (a) and (c) are the images of the $\text{Al}_{0.2}\text{Co}_{1.5}\text{CrFeNi}_{1.5}\text{Ti} + \text{Ag}$ coating at 600 and 750 °C, (b) and (d) corresponding to $\text{Al}_{0.2}\text{Co}_{1.5}\text{CrFeNi}_{1.5}\text{Ti}$ coating at 600 and 750 °C

volume loss mainly came from the oxide layer, for both the HEA and HEA + Ag coating. They obtained a decreased wear rate and friction coefficient, and the wear resistance increased due to the denser, more continuous oxide layer formed and tightly covered on the coating surface, which prevented direct metal–metal contact and adhesive wear. This layer protected the underlying materials from wear loss, and the high hardness value of coating was helpful to improve the wear resistance. Furthermore, the wear rate of HEA + Ag coating was lower compared with HEA at high temperature; this is due to the lubrication of Ag.

4. Discussion

4.1 The Effect of Silver Addition

At 25–400 °C, the HEA + Ag coating had better tribological properties compared with HEA (Fig. 7 and 8), which indicates that silver was the dominant factor in decreasing friction coefficients and wear rate, while the lubrication of Ag reduced the wear debris and decreased friction force. The friction coefficients were decreased from 200 to 750 °C with increasing temperature for both HEA and HEA – Ag coating (Fig. 7). Additionally, the HEA alloy coating obtained a low friction coefficient and a decreased wear rate from 600 to 750 °C, even though there is no silver addition. This indicated that the silver was not the main reason for the friction reduction at 750 °C. Moreover, these results indicated the prepared HEA coating without Ag also had a good lubrication and wear resistance at high temperatures. This is due to the dense, continuous oxide layer formed that tightly covered the coating surface to protect the coating from wear loss and to reduce friction force (Fig. 10). However, the HEA + Ag coating obtained a lower COF and wear rate at high temperatures, which indicated the function of Ag on the anti-friction and wear resistance. The

XRD pattern in Fig. 12 shows the diffraction peaks of the silver phase after friction at 400, 600, and 750 °C, and from the EDS results, the Ag nanoclusters appeared in the precipitated phase on the worn surface at high temperatures.

4.2 Friction-Induced Oxidation

At low temperatures (25–400 °C), friction-induced oxidation occurred during the process of friction. Due to the well mechanical properties and antioxidant properties of the coatings, a thin oxide layer was generated and adhered on the matrix at room temperature. The wear volume loss of the coating mainly came from the oxide layer. However, when temperature rose to 200 °C, a number of cracked and tiny oxide nanoparticles are observed in Fig. 11(b). In fact, the significant oxidation on the wear surface was induced, and the oxidized layers that formed were unable to withstand being worn for a long time at a higher test temperature and friction heat. When the deformation exceeds a certain threshold, the oxidized layer cracked and split from the surface, and thus, the plate-like wear and tiny debris formed. Researchers have shown that delamination of the oxide layer takes place due to internal stress when it reaches a critical thickness (Ref 36). At high temperatures, different wear mechanisms appeared, and the friction-induced metal oxides on the worn surfaces were responsible for low friction and the decreased wear rate of HEA coating at 750 °C. As shown in Fig. 10(a) and (c), a relatively continuous oxide layer was formed on the worn surface at 600 and 750 °C. The smooth oxide layer mainly consisted of Cr₂O₃, Fe₃O₄, NiO, etc., which was revealed by XRD (Fig. 12) and Raman spectrum (Fig. 13). Comparing the element contents of the worn surfaces, oxygen content in the worn surfaces was significantly higher than that in the unworn surface. In addition, the Raman spectrum shows that the oxidization of worn surface was higher than of unworn surface (Fig. 13). Thus, the synergistic effects of Ag and friction-induced oxides were responsible for the favorable tribological performance of the

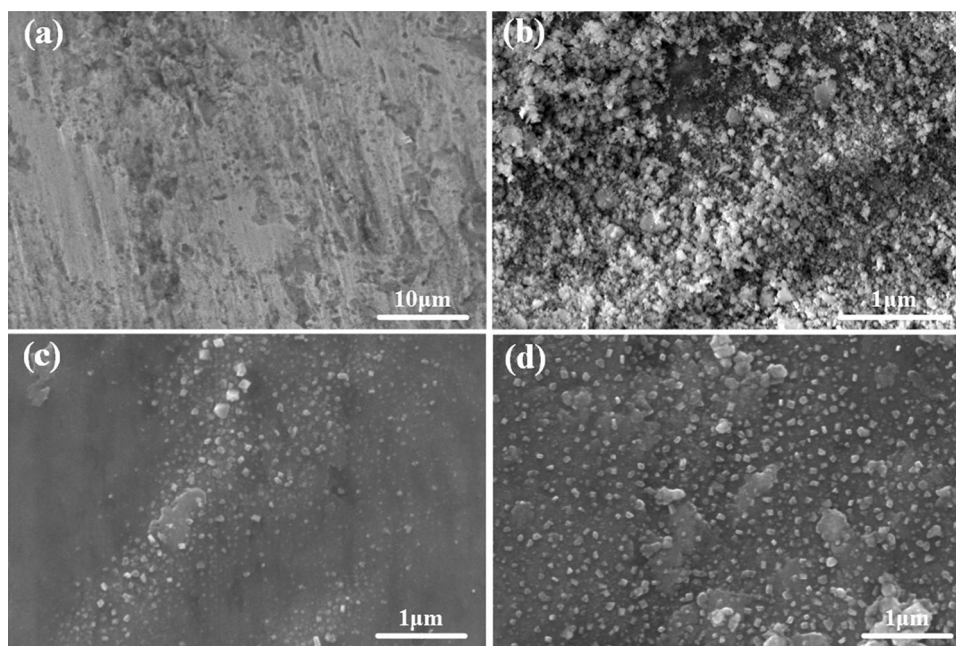


Fig. 11 Worn surface morphologies of HEA – Ag composite coatings with high magnification: (a), (b), (c), and (d) corresponding to 25, 200, 600, and 750 °C

HEA – Ag composite coating at 750 °C. Compared with other reported self-lubricating materials, such as Ni-based composites and Co-based composites, the HEA – Ag composite coating

shows lower friction coefficients and wear rates at high temperatures.

5. Conclusions

$\text{Al}_{0.2}\text{Co}_{1.5}\text{CrFeNi}_{1.5}\text{Ti}$ high-entropy alloy powders with FCC structure by mechanical alloying were successfully prepared by ball milling for 60 h. And then, they were successfully used for preparing silver-containing HEA matrix composite coating by the APS technique. The HEA – Ag coating exhibited higher hardness after annealing at 750 °C due to the oxidation. At low temperatures (RT to 400 °C), the tribological properties of HEA – Ag composite coating depend on their mechanical properties and the lubrication of Ag. The frictional coefficient of HEA – Ag composite coating was lower than of HEA coating. At high temperatures (600–750 °C), both the HEA – Ag and HEA coating obtained good tribological properties; especially, a relatively low wear rate ($8.9 \times 10^{-6} \text{ mm}^3/\text{Nm}$) and friction coefficient (0.253) were achieved at 750 °C for HEA – Ag coating. Finally, a lubricious film that was formed consisted of Ag and various oxides on the frictional surface, which contributed to the outstanding tribological properties.

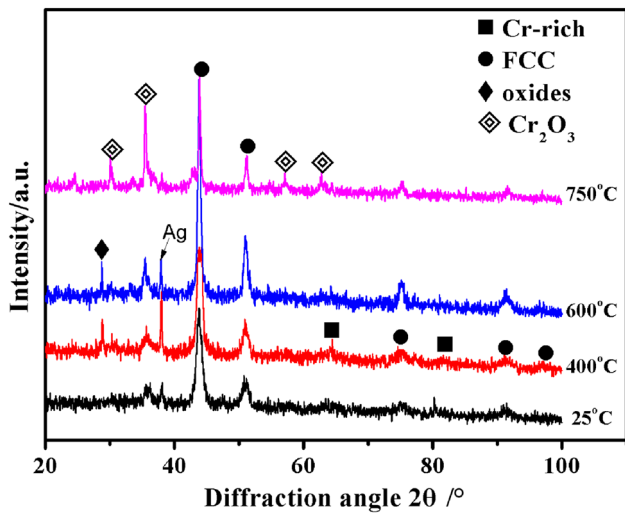


Fig. 12 XRD patterns of the unworn surfaces after wear testing at different temperatures

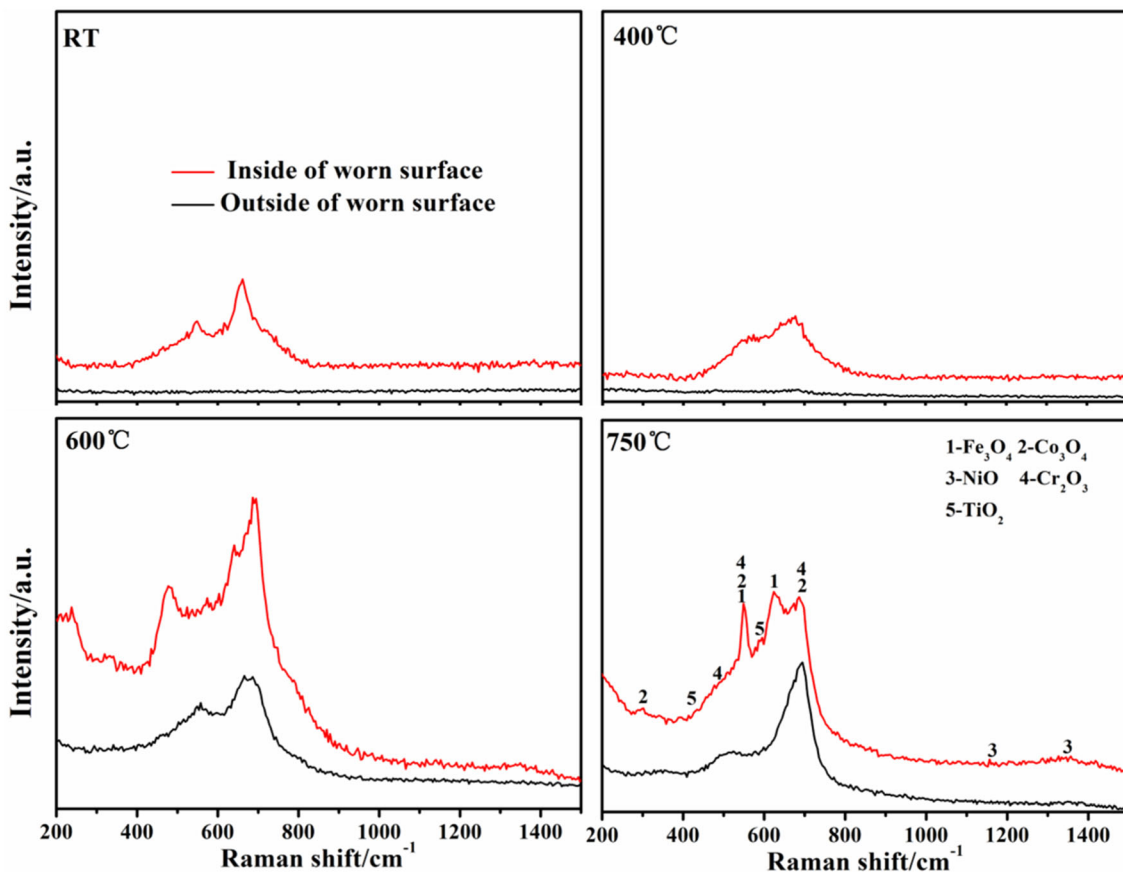


Fig. 13 Raman patterns of worn surfaces at different temperatures: (a), (b), (c), and (d), respectively, corresponding to 25, 400, 600, and 750 °C

Acknowledgments

This work is financially supported by Natural Science Foundation of China (No. 51101087) and Fundamental Research Funds for the Central Universities (No. 30917014106).

References

1. H.E. Sliney, Solid Lubricant Materials for High Temperatures: A Review, *Tribol. Int.*, 1985, **15**(5), p 303–315
2. C.C. Baker, R.R. Chromik, K.J. Wahl et al., Preparation of Chameleon Coatings for Space and Ambient Environments, *Thin Solid Films*, 2007, **515**(17), p 6737–6743
3. W. Wang, Application of a High Temperature Self-lubricating Composite Coating on Steam Turbine Components, *Surf. Coat. Technol.*, 2004, **177**, p 12–17
4. Z. Xu, Q. Zhang, X. Huang et al., An Approximate Model for the Migration of Solid Lubricant on Metal Matrix Self-lubricating Composites, *Tribol. Int.*, 2016, **93**, p 104–114
5. J.E. Mogonye, A. Srivastava, S. Gopagoni et al., Solid/Self-lubrication Mechanisms of an Additively Manufactured Ni-Ti-C Metal Matrix Composite, *Tribol. Lett.*, 2016, **64**(3), p 37
6. H.S. Maharana, A. Basu, and K. Mondal, Structural and Tribological Correlation of Electrodeposited Solid Lubricating Ni-WSe₂ Composite Coating, *Surf. Coat. Technol.*, 2018, **349**, p 328–339
7. J. Zhen, J. Cheng, M. Li et al., Lubricating Behavior of Adaptive Nickel Alloy Matrix Composites with Multiple Solid Lubricants from 25 to 700 °C, *Tribol. Int.*, 2017, **109**, p 174–181
8. B. Li, J. Jia, Y. Gao et al., Microstructural and Tribological Characterization of NiAl Matrix Self-lubricating Composite Coatings by Atmospheric Plasma Spraying, *Tribol. Int.*, 2017, **109**, p 563–570
9. Y. Xiao, X. Shi, W. Zhai et al., Effect of Temperature on Tribological Properties and Wear Mechanisms of NiAl Matrix Self-lubricating Composites Containing Graphene Nanoplatelets, *Tribol. Trans.*, 2015, **58**(4), p 729–735
10. S. Zhu, F. Li, J. Ma et al., Tribological Properties of Ni3Al Matrix Composites with Addition of Silver and Barium Salt, *Tribol. Int.*, 2015, **84**, p 118–123
11. M.H. Chuang, M.H. Tsai, W.R. Wang et al., Microstructure and Wear Behavior of Al_xCo_{1.5}CrFeNi_{1.5}Ti_y High-Entropy Alloys, *Acta Mater.*, 2011, **59**, p 6308–6317
12. C.J. Tong, Y.L. Chen, J.W. Yeh et al., Microstructure Characterization of Al_xCoCrCuFeNi High-Entropy Alloy System with Multiprincipal Elements, *Metall. Mater. Trans. A*, 2005, **36**(4), p 881–893
13. X.W. Qiu and C.G. Liu, Microstructure and Properties of Al₂CrFeCo-CuTiNi_x High-Entropy Alloys Prepared by Laser Cladding, *J. Alloys Compd.*, 2013, **553**, p 216–220
14. S. Zhang, C.L. Wu, J.Z. Yi et al., Synthesis and Characterization of FeCoCrAlCu High-Entropy Alloy Coating by Laser Surface Alloying, *Surf. Coat. Technol.*, 2015, **262**, p 64–69
15. S. Varalakshmi, G.A. Rao, M. Kamaraj et al., Hot Consolidation and Mechanical Properties of Nanocrystalline Equiatomic AlFeTiCrZnCu High Entropy Alloy after Mechanical Alloying, *J. Mater. Sci.*, 2010, **45**(19), p 5158–5163
16. F. He, Z. Wang, Q. Wu et al., Phase Separation of Metastable CoCrFeNi High Entropy Alloy at Intermediate Temperatures, *Scr. Mater.*, 2017, **126**, p 15–19
17. S. Praveen, J. Basu, S. Kashyap et al., Exceptional Resistance to Grain Growth in Nanocrystalline CoCrFeNi High Entropy Alloy at High Homologous Temperatures, *J. Alloys Compd.*, 2016, **662**, p 361–367
18. S. Jiang, Z. Lin, H. Xu et al., Studies on the Microstructure and Properties of Al_xCoCrFeNiTi_{1-x} High Entropy Alloys, *J. Alloys Compd.*, 2018, **741**, p 826–833
19. T. Fujieda, H. Shiratori, K. Kuwabara et al., CoCrFeNiTi-Based High-Entropy Alloy with Superior Tensile Strength and Corrosion Resistance Achieved by a Combination of Additive Manufacturing Using Selective Electron Beam Melting and Solution Treatment, *Mater. Lett.*, 2017, **189**, p 148–151
20. T.T. Shun, L.Y. Chang, and M.H. Shiu, Microstructures and Mechanical Properties of Multiprincipal Component CoCrFeNiTi_x Alloys, *Mater. Sci. Eng., A*, 2012, **556**, p 170–174
21. P.K. Huang, J.W. Yeh, T.T. Shun et al., Multi Principal Element Alloys with Improved Oxidation and Wear Resistance for Thermal Spray Coating, *Adv. Eng. Mater.*, 2004, **6**(1–2), p 74–78
22. D.J.M. King, S.C. Middleburgh, A.G. McGregor et al., Predicting the Formation and Stability of Single Phase High-Entropy Alloys, *Acta Mater.*, 2016, **104**, p 172–179
23. A.S.M. Ang, C.C. Berndt, M.L. Sesso et al., Plasma-Sprayed High Entropy Alloys: Microstructure and Properties of AlCoCrFeNi and MnCoCrFeNi, *Metall. Mater. Trans. A*, 2015, **46**(2), p 791–800
24. W. Ji, W. Wang, H. Wang et al., Alloying Behavior and Novel Properties of CoCrFeNiMn High-Entropy Alloy Fabricated by Mechanical Alloying and Spark Plasma Sintering, *Intermetallics*, 2015, **56**, p 24–27
25. P.F. Yu, L.J. Zhang, H. Cheng et al., The High-Entropy Alloys with High Hardness and Soft Magnetic Property Prepared by Mechanical Alloying and High-Pressure Sintering, *Intermetallics*, 2016, **70**, p 82–87
26. L.S. Wang, S.L. Zhang, T. Liu et al., Dominant Effect of Particle Size on the CeO₂ Preferential Evaporation During Plasma Spraying of La₂Ce₂O₇, *J. Eur. Ceram. Soc.*, 2017, **37**(4), p 1577–1585
27. I. Hwang, J. Jeong, K. Lim et al., Microstructural Characterization of Spray-Dried NiO-8YSZ Particles as Plasma Sprayable Anode Materials for Metal-Supported Solid Oxide Fuel Cell, *Ceram. Int.*, 2017, **43**(10), p 7728–7735
28. S. Sivakumar, K. Praveen, and G. Shanmugavelayutham, Preparation and Thermophysical Properties of Plasma Sprayed Lanthanum Zirconate, *Mater. Chem. Phys.*, 2018, **204**, p 67–71
29. J.W. Yeh, S.Y. Chang, Y.D. Hong et al., Anomalous Decrease in X-Ray Diffraction Intensities of Cu-Ni-Al-Co-Cr-Fe-Si Alloy Systems with Multi-principal Elements, *Mater. Chem. Phys.*, 2007, **103**(1), p 41–46
30. H.X. Sui, M. Zhu, M. Qi et al., Erratum: The Enhancement of Solid Solubility Limits of AlCo Intermetallic Compound by High-Energy Ball Milling, *J. Appl. Phys.*, 1993, **71**, p 2945
31. B.L. Huang, R.J. Perez, E.J. Lavernia et al., Formation of Supersaturated Solid Solutions by Mechanical Alloying, *Nanostruct. Mater.*, 1996, **7**, p 67–79
32. A.R. Yavari, P.J. Desrā, and T. Benameur, Mechanically Driven Alloying of Immiscible Elements, *Phys. Rev. Lett.*, 1992, **68**(14), p 2235–2238
33. S. Guo, C. Ng, Z. Wang et al., Solid Solutioning in Equiatomic Alloys: Limit Set by Topological Instability, *J. Alloys Compd.*, 2014, **583**(1), p 410–413
34. K. Radil and C. DellaCorte, The Performance of PS400 Subjected to Sliding Contact at Temperatures from 260 to 927 K, *Tribol. Trans.*, 2017, **60**(6), p 957–964
35. C.D. Corte, M.K. Stanford, F. Thomas, and B.J. Edmonds, “The Effect of Composition on the Surface Finish of PS400: A New High Temperature Solid Lubricant Coating,” NASA-TM-2010-216774, 2010
36. F.H. Stott, The Role of Oxidation in the Wear of Alloys, *Tribol. Int.*, 1998, **31**(1–3), p 61–71. [https://doi.org/10.1016/S0301-679X\(98\)00008-5](https://doi.org/10.1016/S0301-679X(98)00008-5)

Publisher's Note Springer Nature remains neutral with regard to jurisdictional claims in published maps and institutional affiliations.